NJC

PAPER

View Article Online
View Journal | View Issue



Cite this: *New J. Chem.*, 2025, **49**, 16617

# Fabrication of three-dimensionally ordered mesoporous zirconia using nanoporous carbon as a scaffold

Takamichi Matsuno, *[abc] Gen Koinuma,[a] Hiroaki Wada,[a] Atsushi Shimojima [abc] and Kazuyuki Kuroda [ab]

Received 2nd April 2025,
Accepted 17th August 2025

DOI: 10.1039/d5nj01465d

rsc.li/njc

Zirconia exhibits important properties such as catalytic activity, ionic conductivity, and dielectric properties. Nanoporous zirconia, with its high surface area and large pore volume, is attracting attention for catalysts and separation materials. Precise pore size control is crucial for the applications; however, achieving control within the range of tens of nm remains difficult. In this study, znanoporous carbon was used as a nanoscale scaffold onto which Zr species were deposited with nanometer thickness, followed by calcination for carbon removal and zirconia crystallization, thereby yielding ordered nanoporous zirconias. This process is crucial for forminghighly ordered nanoporous zirconias with improved pore size control and uniformity.



## Introduction

Among transition metal oxides, zirconia has been widely studied and applied based on its properties, such as high chemical and thermal stability,[1] high hardness and strength,[1] acidic and basic catalytic activities,[2] ionic conductivity,[3] and dielectric properties.[3] The typical crystal phases of zirconia include monoclinic, tetragonal, and cubic polymorphs, which are known to have different catalytic activity and selectivity.[4–6] Nanoporous zirconia combines the aforementioned characteristics of zirconia with the features of high specific surface area and high pore volume typical of nanoporous materials and is attracting particular attention in applications for catalysts, catalyst supports,[7] and separation and purification materials.[8] Zirconium alkoxide and $ZrOCl_2{\cdot}8H_2O$ are mainly used as Zr sources, and nanoporous zirconia with various porous structures and pore diameters has been synthesized.[9–21] In particular, mesoporous zirconia with pores of a few nanometers in diameter has been studied for the hydrogenation of unsaturated alcohols[9] and adsorption of heavy metals[10] by taking advantage of its high surface area and large pore volume. Macroporous zirconia with a pore size of several hundred nanometers has been reported as a support of $Au@CeO_{2-\delta}$ catalysts[22] for the combustion of soot particles (several tens of nm in size) in exhaust gases, taking advantage of its large pore size. In addition, it has recently been reported that electronic interactions between the catalyst and the support have a significant effect on the catalytic activity of metal and metal oxide nanoparticles supported on zirconia.[23] The improvement in selectivity and catalytic activity for specific reactions, such as the conversion of $CO_2$ to methanol,[23] suggests that nanoporous zirconia plays a significant role in the catalytic mechanism, in addition to contributing as a catalyst support with a high surface area and durability. For the study of these applications, broad pore size control from meso to macro scale is crucial for understanding the correlation between catalytic activity and factors such as specific surface area, reactant size, and mass diffusivity.[24]

Mesoporous zirconia with pore diameter of several nanometers has been prepared using surfactant micelles[11,12] and mesoporous silica[13,14] as templates, while the formation of nanopores of several hundred nanometers is achieved using polymer particles as templates.[15–17] However, these methods are not suitable for controlling the pore size in the intermediate range from low tens of nanometers to several tens of nanometers, and the preparation of mesoporous zirconia with pore sizes in this region has been limited.[20,21] In previous reports, assemblies of silica nanospheres were used as templates to produce mesoporous zirconia. Randomly arranged spherical pores were formed using randomly assembled silica nanospheres,[20] while an inverse opal structure was formed using silica colloidal crystals (SCCs) with face-centered cubic (fcc)-packed silica nanospheres.[21] However, the smallest size of

[a] *Department of Applied Chemistry, Faculty of Science and Engineering, Waseda University, 3-4-1 Okubo, Shinjuku-ku, Tokyo 169-8555, Japan. E-mail: matsuno@aoni.waseda.jp*
[b] *Kagami Memorial Research Institute for Materials Science and Technology, Waseda University, 2-8-26 Nishiwaseda, Shinjuku-ku, Tokyo, 169-0051, Japan*
[c] *Waseda Research Institute for Science and Engineering, Waseda University, 3-4-1 Okubo, Shinjuku-ku, Tokyo 169-8555, Japan*

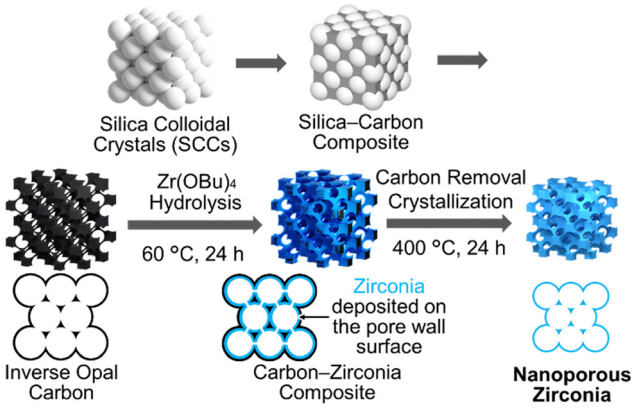


Scheme 1 Preparation of three-dimensionally ordered nanoporous zirconia using a porous carbon scaffold. Inverse opal carbon was prepared by depositing carbon in the interstitial nanopores of SCCs and then removing silica. $Zr(OBu)_4$ solution was infiltrated into the inverse opal carbon to precipitate Zr species on the pore wall surface. Carbon removal and crystallization of zirconia were accomplished through calcination, resulting in the formation of nanoporous zirconia.

applied silica nanosphere was 34 nm,[21] and the pore size distribution of mesoporous zirconia calculated from $N_2$ adsorption–desorption isotherms was broad. Therefore, nanoporous zirconia with well-controlled pore sizes in the range of low tens of nanometers to several tens of nanometers is still a *missing link*.

In this study, three-dimensionally ordered nanoporous zirconia with a pore size range from low tens of nanometers to several tens of nanometers was prepared by precipitating zirconia onto the pore walls of nanoporous carbon (Scheme 1). Generally, inverse replicas are obtained when nanoporous materials are used as templates,[25] although replication from one inverse opal structure to another has been reported on a larger scale in pore diameter (~300 nm).[17] Using our present method, we succeeded in replicating the template structure across the meso to macro scale by uniformly and thinly coating zirconia on the surface of a carbon template at the nano-level with a simple incipient wetness infiltration method, thereby achieving high porosity and uniform nanopores. The uniform zirconia coating was achieved by using a zirconium butoxide 1-butanol solution as a precursor, which has a relatively low surface tension and is believed to spread thinly on hydrophobic carbon surfaces. The nanoporous zirconia obtained *via* hydrolysis, condensation, and calcination exhibited narrow pore size distributions, confirming the preparation of nanoporous zirconia with higher regularity over a broader range of pore sizes than previous methods.

## Experimental section

### Materials

Tetraethoxysilane (TEOS) was purchased from Kishida Chemical Co., Ltd. Tris(hydroxymethyl)aminomethane (THAM), sucrose, sulfuric acid (>95.0%), 2 M sodium hydroxide (NaOH) aq., zirconium(iv) oxychloride octahydrate ($ZrOCl_2 \cdot 8H_2O$) were purchased from FUJIFILM Wako Pure Chemical Corporation. Zirconium(iv) butoxide ($Zr(OBu)_4$) 1-butanol solution (~80%) and titanium tetraisopropoxide ($Ti(O\text{-}iPr)_4$) were purchased from Tokyo Chemical Industry Co., Ltd. Ethanol was purchased from Junsei Chemical Co., Ltd. All reagents were used as received.

### Preparation of silica colloidal crystals (SCCs)

Colloidal silica nanospheres and SCCs were prepared according to our previous reports.[26,27] Colloidal silica nanospheres with an average particle size of 28 nm were prepared as follows. 250 mL of a 0.2 M THAM solution was heated and stirred (80 °C, 850 rpm). 199 mL of TEOS was then added to the solution and the mixture was stirred at 80 °C for 24 h (TEOS : THAM : $H_2O$ = 90 : 5 : 1390). The size of the obtained silica nanospheres was increased by a seed growth method to obtain colloidal silica nanospheres with 66 nm and 109 nm in diameter (the average diameter of the silica nanospheres is the average of 200 diameters measured from TEM images). 0.2 M THAM solution was added to the aliquoted silica nanosphere dispersion (seed dispersion) and the mixture was stirred at 80 °C. After the temperature reached a steady state, TEOS was added and subsequently heated and stirred at 80 °C for 24 h. The detailed conditions are described in Table S1, SI. The molar ratio of TEOS, THAM, and $H_2O$ in the sample was set to be the same as in the seed solution (TEOS : THAM : $H_2O$ = 90 : 5 : 1390), and the amount of TEOS to be added ($TEOS_{add}$) was calculated from the following formula (details are described in SI).

$$TEOS_{add} = TEOS_{seed} \times ({D_{obj}}^3/{D_{seed}}^3 - 1)$$

($TEOS_{seed}$ is the amount of TEOS used in the preparation of seed nanospheres (mL); $D_{obj}$ is the objective diameter (nm); $D_{seed}$ is the diameter of seed nanospheres (nm)).

The resulting silica nanosphere dispersions were dried and calcined at 600 °C in air for 6 h (temperature rise and fall rate is 1.6 °C $min^{-1}$) to remove THAM and obtain SCCs (sample names are denoted as SCC-*x*, where *x* is the sphere size). The characterization of the SCCs is shown in SI.

### Preparation of inverse opal carbons

Nanoporous carbons with inverse opal structure were prepared using SCCs as templates. SCCs were dried at 120 °C for 3 h before use. An aqueous solution of sucrose (0.553 g sucrose was dissolved in 0.7 mL pure water) with 32.4 μL of sulfuric acid was infiltrated into 3 g of SCCs. Then, the composites were heated at 100 °C for 5 h and subsequently at 150 °C for 12 h, and the sucrose was carbonized by heating in an Ar flow at 900 °C for 6 h (both heating and cooling rates were 1.8 °C $min^{-1}$). The resulting black powder was added to 400 mL of 2 M NaOH solution and stirred at 80 °C for 24 h to remove silica. The process was then repeated twice for filtration and redispersion in water for washing. The solid samples were collected by filtration and dried to obtain inverse opal carbon (IOC-*x*, where *x* is the pore size). The characterization of the samples is shown in SI.

 

**Fabrication of mesoporous zirconia and macroporous zirconia using inverse opal carbons as scaffolds**

0.05 g of nanoporous carbon (IOC-28, 66, or 109) was vacuum-dried at 120 °C for 3 h in a 50 mL recovery flask, and dried $N_2$ was introduced. 200 μL of $Zr(OBu)_4$ butanol solution was added and mixed to infiltrate the entire solution. The amount of $Zr(OBu)_4$ butanol solution added was set to ~60% of the pore volume to prevent precipitation outside the carbon template. Subsequent heating in air at 60 °C for 24 h (the room condition was 22 °C and ~30% relative humidity) allowed the hydrolysis of $Zr(OBu)_4$ by atmospheric moisture to yield carbon–zirconia nanocomposites (C–$ZrO_2$-*x*, *x* = 28, 66, and 109). The resulting carbon–zirconia composite was transferred to an alumina boat and calcined in air at 400 °C for 24 h to remove the carbon and to proceed with the crystallization of zirconia, yielding nanoporous zirconia (P-$ZrO_2$-*x*, *x* = 28, 66, and 109, corresponding to the pore sizes of the carbon templates).

## Results and discussions

**Characterization of the carbon–zirconia nanocomposite**

Detailed characterization and discussions are presented for a system using IOC-66 as a template, which produced mesoporous zirconia with particularly high structural regularity. In this section, the chemical state and distribution of Zr species in C–$ZrO_2$-66, a composite of carbon template and zirconia, are presented. The detailed characterization of SCCs-*x* and IOC-*x* used in the preparation of the template is shown in the SI (Fig. S1–S4). IOC-66 is a carbon with an inverse opal structure and a pore size of ~66 nm.

The powder XRD pattern of C–$ZrO_2$-66 (Fig. 1a) displays broad peaks derived from amorphous carbon as well as broad peaks similar to those of tetragonal $ZrO_2$ (t-$ZrO_2$, ICDD card no. 00-050-1089), indicating that the sample is poorly crystalline.

In the FT-IR spectrum of C–$ZrO_2$-66 (Fig. S5, SI), a broad C–O stretching[28] band around 1200 $cm^{-1}$ and a C=C stretching[28] band around 1600 $cm^{-1}$ were observed, as in the carbon template. The slight absorption band around 500 $cm^{-1}$ is attributed to the Zr–O vibration[18] of the Zr–O–Zr bond. When considered together with the FT-IR spectrum of hydrolyzed-$Zr(OBu)_4$, which was obtained without using a template, the weak absorption intensity of the Zr–O–Zr bond in C–$ZrO_2$-66 may be due to absorption by carbon. In the IR spectrum of hydrolyzed-$Zr(OBu)_4$, absorption bands arising from the $–CH_2–$ and $–CH_3$ groups of butanol and butoxy groups, as well as those from C–OH and C–O–Zr groups,[29,30] were not observed, suggesting that hydrolysis and polycondensation occurred sufficiently. The absorption bands at 1340 and 1550 $cm^{-1}$ are attributed to Zr–OH vibrations.[31,32] TG-DTA measurements of hydrolyzed-$Zr(OBu)_4$ showed a weight loss of about 27% (Fig. S6a, SI). Considering that a 23% weight loss occurs during the dehydration and condensation of $Zr(OH)_4$ to $ZrO_2$, the observed 27% weight loss is attributed to the dehydration of adsorbed water and additional dehydration condensation, suggesting that the composition is close to $ZrO_2$. Hydrolysis and polycondensation of $Zr(OBu)_4$ are thought to proceed similarly in the carbon template, forming a poorly crystalline zirconium oxide containing Zr–OH.

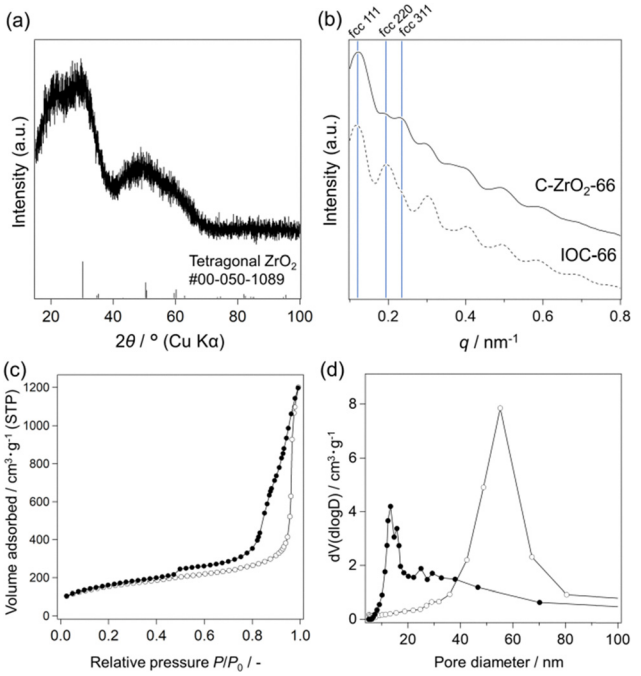


Fig. 1 (a) XRD pattern (bottom: simulated pattern), (b) SAXS pattern, (c) $N_2$ adsorption–desorption isotherms, and (d) BJH pore diameter distributions of C–$ZrO_2$-66 (○: adsorption, ●: desorption).

The SEM image of C–$ZrO_2$-66 (Fig. 2a) shows an increase in the pore wall thickness of the porous carbon (Fig. S3c, SI). The TEM image (Fig. 2b) revealed that the pore wall surface of the inverse opal carbon was coated with a layer several nanometers thick that exhibited different contrast (the region surrounded by the yellow dotted lines). In addition, the contrast was uniform throughout the particles (TEM, Fig. 2c). The HAADF-STEM image of C–$ZrO_2$-66 (Fig. 2d) also showed a porous structure with spherical nanopores similar to that of the inverse opal carbon. EDS elemental mapping of the same view (Fig. 2e–g) shows that carbon and Zr are uniformly present in the pore wall region. In the carbon mapping, the contrast is stronger in the regions where the pore walls are thicker, such as the octahedral and tetrahedral sites in the fcc structure. However, Zr species are uniformly distributed, showing no preference for either octahedral or tetrahedral sites. This is particularly obvious in the overlaid image (Fig. 2g). This result indicates that Zr species uniformly coat the pore wall surface of the nanoporous carbon.

The $N_2$ adsorption–desorption isotherms of C–$ZrO_2$-66 (Fig. 1c) were type IV(a), as in the case of the inverse opal carbon (Fig. S4, SI), but the drop in the desorption isotherm from $P/P_0$ = 0.9 to 0.8 was gradual, and a steep drop was observed at a relative pressure of 0.45 due to cavitation. The pore size distribution was calculated by the BJH method (Fig. 1d), and a peak at ~60 nm was observed from the adsorption isotherm, which is close to that of the inverse opal carbon. Using the desorption isotherm, a broad peak from 18 to 60 nm was observed. These results suggest

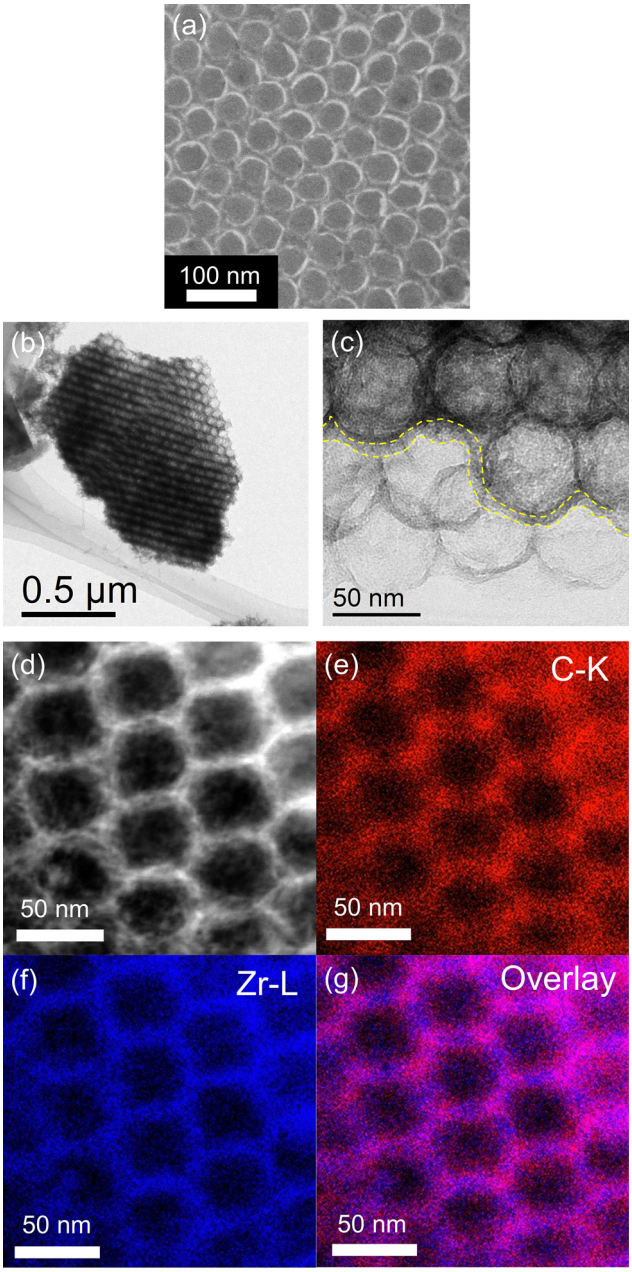


Fig. 2 (a) SEM image, (b) and (c) TEM images, (d) HAADF-STEM image, and (e–g) EDS elemental mapping of C–$ZrO_2$-66. The yellow dotted lines in (c) visualize the boundary of the contrast.

that the window pores connecting the spherical pores became smaller due to the deposition of zirconia on the pore wall surface. The most important point derived from the $N_2$ adsorption–desorption measurement is that zirconia does not fill the window pores of the inverse opal carbon.

The T-SAXS pattern of C–$ZrO_2$-66 (Fig. 1b) shows peaks at the same $q$ values as those of the inverse opal carbon, confirming that the pore structure is unchanged. However, the peak intensity of the 220 diffraction of the fcc structure decreased, while that of the 311 diffraction increased relatively. This change could be caused by the uniform coating of zirconia on the carbon. The presence of zirconium oxide, with a relatively high electron density, on the carbon surface may have caused a change in the scattering intensity of each diffraction, but the details are uncertain.

The above results collectively confirm that zirconium oxide uniformly coated the pore wall surface of the inverse opal carbon. The factors contributing to the uniform coverage are considered to be the low surface tension of the $Zr(OBu)_4$ 1-butanol solution and its affinity for the hydrophobic carbon surface. As a result, the $Zr(OBu)_4$ solution introduced into the pores was able to wet the pore wall surface uniformly, and hydrolysis and polycondensation of $Zr(OBu)_4$ on the pore wall progressed.

### Template removal and crystallization of zirconia during the calcination process

TG-DTA measurement of C–$ZrO_2$-66 was performed to clarify the process of $ZrO_2$ crystallization and template removal (Fig. S6b, SI). C–$ZrO_2$-66 was heated to 300 °C at 1.7 °C $min^{-1}$ (same rate as the template removal condition) and then held at 300 °C for 18 h. As a result, a weight loss accompanied by a sharp exothermic peak at ~300 °C was observed, which is attributed to the combustion of the template carbon. In contrast, when solely the porous carbon was examined, a weight loss was observed but with a relatively small exothermic peak (Fig. S6c, SI). No such sharp exothermic peak was observed for hydrolyzed-$Zr(OBu)_4$ (Fig. S6a, SI). These results suggest that the template carbon combusted intensely in the carbon–$ZrO_2$ complex despite the relatively low temperature, possibly due to $ZrO_2$ catalyzing the combustion reaction of carbon.[33] The TG-DTA results for hydrolyzed-$Zr(OBu)_4$ indicate a weight loss at ~350 °C, which is attributed to the condensation of ZrOH. These findings suggest that carbon was removed up to ~300 °C, and zirconia crystallized either subsequently or simultaneously.

### Characterization of the three-dimensionally ordered mesoporous zirconia

After calcination at 400 °C, the resulting P-$ZrO_2$-66 appeared as a white powder, with CHN elemental analysis confirming that the residual carbon was less than 1 wt%. The powder XRD pattern (Fig. 3a) displays diffraction peaks corresponding to t-$ZrO_2$ and those attributable to monoclinic $ZrO_2$ (m-$ZrO_2$) as a minor phase. The crystallite size calculated from the 011 diffraction using the Scherrer equation (constant $K$ = 0.9) was 7.5 nm. The FT-IR spectrum (Fig. S5, SI) shows absorption bands originating from Zr–O–Zr vibrations below 1000 $cm^{-1}$ and from Zr–OH vibrations around 1340 $cm^{-1}$, similar to the FT-IR spectrum of hydrolyzed-$Zr(OBu)_4$ (Fig. S5, SI).

SEM and TEM images (Fig. 4a–d) show that the porous structure of the inverse opal carbon with regularly arranged spherical pores was replicated. The pore size was ~40 nm, approximately a 40% decrease from that of the inverse opal carbon (66 nm). The SAED patterns (Fig. 4c) display ring patterns assigned to t-$ZrO_2$. The lattice fringe observed in the high-magnification TEM image (Fig. 4d) confirmed that the pore walls were composed of microcrystalline $ZrO_2$ with sizes of

 

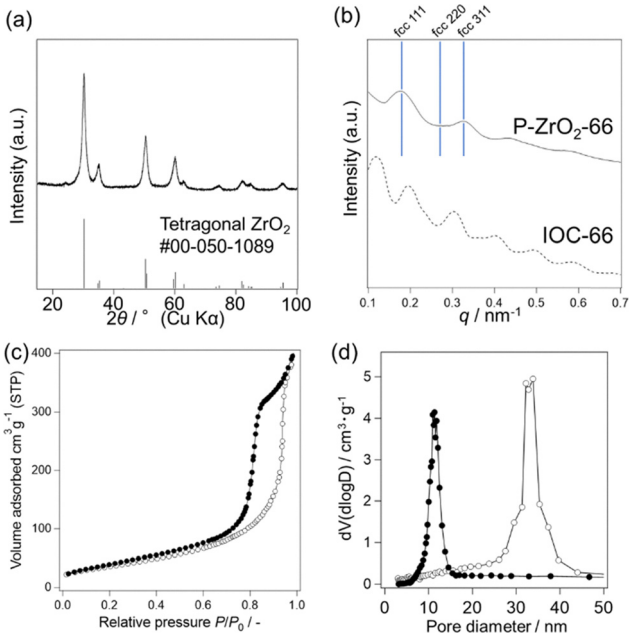


Fig. 3 (a) XRD pattern, (b) SAXS pattern, (c) $N_2$ adsorption–desorption isotherms, and (d) BJH pore diameter distributions of P-$ZrO_2$-66 (○: adsorption, ●: desorption).

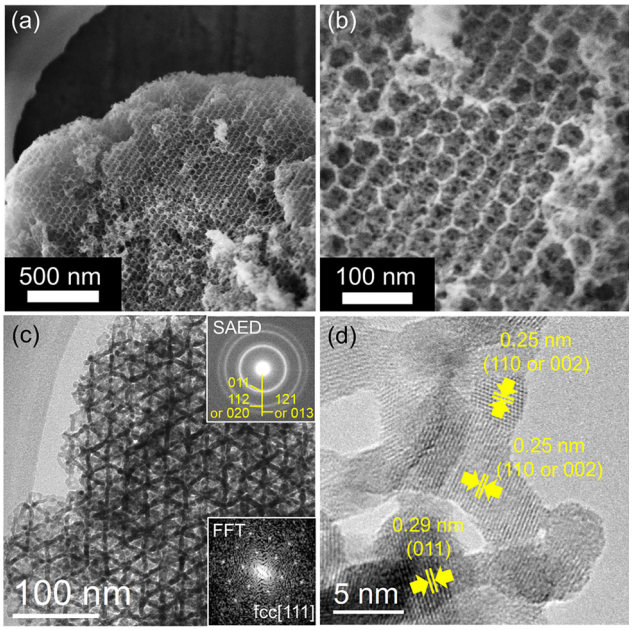


Fig. 4 (a) and (b) SEM images and (c) and (d) TEM images of P-$ZrO_2$-66 (insets: SAED pattern and FFT pattern).

a few nanometers, which is close to the crystallite size estimated from the XRD results.

The T-SAXS pattern of P-$ZrO_2$-66 (Fig. 3b) shows peaks attributable to an fcc structure, confirming that the porous structure of IOC-66 was replicated. In addition, peak shifts to higher angles compared to IOC-66 were observed, confirming a ~40% shrinkage of the structural period. This volume shrinkage is likely caused by the removal of the scaffold carbon and is consistent with shrinkage estimates from electron microscopy observations. Similar to C–$ZrO_2$-66, the 220 diffraction intensity was weaker than that of IOC-66, suggesting that the porous structure deviates from an ideal inverse opal structure. Since the volume of tetrahedral and octahedral sites was observed to be significantly smaller than that of the IOC-66 from the TEM image (Fig. 4c), it is possible that the scattering intensity derived from these sites is changed, resulting in the characteristic SAXS pattern.

Based on the $N_2$ adsorption–desorption measurement (Fig. 3c), an uptake near $P/P_0$ = 0.9 on the adsorption isotherm and a steep drop near $P/P_0$ = 0.8 on the desorption isotherm were observed. The BET specific surface area and pore volume were calculated to be 133 $m^2\ g^{-1}$ and 0.64 $cm^3\ g^{-1}$, respectively. Although the BET area is not particularly high compared to that of previously reported mesoporous $ZrO_2$, the pore volume is larger[14] because of the porous structure similar to the inverse opal structure. The BET area and pore volume are much larger than the calculated values for the ideal inverse opal structure (70 $m^2\ g^{-1}$ and 0.47 $cm^3\ g^{-1}$). This is because the mesoporous zirconia produced is composed of small crystallites, resulting in high surface roughness and thin pore walls. The BJH method (Fig. 3d) confirmed that the pore size distribution was relatively narrow, indicating the formation of uniform nanopores. Peaks were observed at around 33 nm from the adsorption isotherm and at 11 nm from the desorption isotherm. The 33 nm pore is several nanometers smaller than the spherical pore size observed by electron microscopy, suggesting that the pore size was underestimated. The 11 nm pore is thought to originate from window pores connecting spherical pores.

Based on the above results, the preparation of three-dimensionally ordered mesoporous zirconia with regularly arranged spherical pores of ~40 nm in diameter was confirmed. The mesopores are more uniform compared to those reported previously using SCCs as a template.[21] This difference may be due to variations in the formation process of mesoporous zirconia. In previous studies using SCCs as templates, zirconia microcrystals were formed by thermal decomposition of the precursor in the confined nanospaces of a rigid template, resulting in poor contact between crystallites due to volume shrinkage, and the structure may have collapsed when the template was removed (Fig. 5, top) (the experimental results are shown later). On the other hand, in the present system using nanoporous carbon as a scaffold, the volume decreases by carbon removal, resulting in the formation of three-dimensional continuous pore walls composed of poorly crystalline zirconia. The subsequent crystallization process facilitates the formation of well-connected zirconia crystallites (Fig. 5, bottom).

The above results are expected to be useful in investigating the correlation between pore size and catalytic activity in the future. This synthesis method is also considered effective for compositions that are difficult to prepare using silica as a template. For example, this method can be applied to silica and titania (TEOS and $Ti(O\text{-}iPr)_4$ were used instead of $Zr(OBu)_4$)

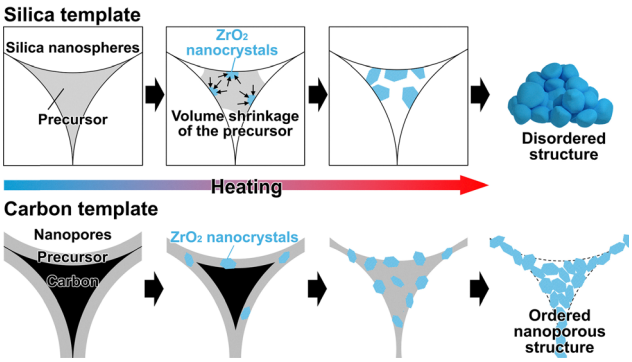


Fig. 5 Schematic image of the presumed crystallization and template removal process using silica or carbon templates.

to prepare three-dimensionally ordered mesoporous materials (Fig. S7, SI). Because it is difficult to control the pore size in the range of several tens of nanometers in both cases, this method is expected to extend the scope of ordered nanoporous metal-oxide materials. In previously, control over pore size and pore wall thickness using persistent micelle templates or block copolymer templates has been reported for aluminosilicate, $TiO_2$, $Nb_2O_5$ and niobium tungsten oxide.[34,35] These methods offer advantages in that mesostructures can be formed through the mixing of templates and precursors, followed by self-assembly, and a variety of pore architectures can be achieved. In contrast, the present method offers several advantages. First, it does not require the synthesis of block copolymers and instead relies on a simple sol–gel reaction followed by heating and calcination. Second, it eliminates the need to adjust the interactions between precursors and block copolymers or micelles in solution depending on composition, which may allow broader applicability to various inorganic oxides. Furthermore, because the structure of monodispersed silica nanospheres is replicated, precise control over the pore size distribution and the structural order can be achieved.

### Control of the pore size in the range of meso- to macro-porous scale

P-$ZrO_2$-28 and P-$ZrO_2$-109 were prepared using porous carbons (IOC-28 and IOC-109) with different pore diameters to investigate the range in which this method can be applied. HAADF-STEM images of C–$ZrO_2$-28 and C–$ZrO_2$-109 (Fig. S8a and e, SI) showed a three-dimensionally ordered structure similar to that of C–$ZrO_2$-66. The Zr species were homogeneously distributed on the surface of the nanoporous carbon, as confirmed by EDS mapping of the same field of view (Fig. S8b–d and f–h, SI). The SAXS pattern (Fig. S9, SI) also resembles that of C–$ZrO_2$-66, with peaks originating from the fcc structure and a weak 220 diffraction peak observed. These results indicate that the pore wall surface can be coated with zirconia over a pore size range of approximately 30–110 nm.

After calcination, both samples, P-$ZrO_2$-28 and P-$ZrO_2$-109, were obtained as white powders. Powder XRD patterns (Fig. S10a and b, SI) show that the major peaks are assigned to t-$ZrO_2$, and the crystallite sizes of P-$ZrO_2$-28 and P-$ZrO_2$-109 are 6.8 nm and 7.5 nm, respectively, which are similar to the crystallite size of P-$ZrO_2$-66 as calculated by the Scherrer equation. Peaks attributable to m-$ZrO_2$ were also observed as a minor phase.

The SEM (Fig. 6a and c) and TEM (Fig. 6b and d) images of both samples show regularly arranged spherical nanopores, indicating successful replication of the porous structure of the template. The SAED patterns are ring patterns assignable to t-$ZrO_2$ in both samples. The respective pore diameters estimated from the TEM images were 14 nm (P-$ZrO_2$-28) and 74 nm (P-$ZrO_2$-109), indicating shrinkage of the structure. For P-$ZrO_2$-28, although the ordered porous structure derived from the template carbon was observed, some regions exhibited less regularity (SEM, Fig. S11, SI).

In the T-SAXS patterns of P-$ZrO_2$-28 and P-$ZrO_2$-109 (Fig. S9, SI), retention of the fcc structure was confirmed. The calculated distances between nanopore centers in P-$ZrO_2$-28 and P-$ZrO_2$-109 are 16 nm and 82 nm, respectively, which are about 43% and 25% smaller than the pore sizes of the template carbon, respectively. These results are consistent with the SEM and TEM observations.

$N_2$ adsorption–desorption measurements of P-$ZrO_2$-28 and P-$ZrO_2$-109 show type IV(a) isotherms, and the BJH pore size distributions confirmed the presence of uniform mesopores (Fig. S10c–f, SI). Steep uptake and drop were observed in both samples as well as in P-$ZrO_2$-66. BET area and pore volime were calculated to be 121 $m^2\ g^{-1}$ and 0.3 $cm^3\ g^{-1}$ (P-$ZrO_2$-28), and 90 $m^2\ g^{-1}$ and 0.7 $cm^3\ g^{-1}$ (P-$ZrO_2$-109). The BET area and pore volume of P-$ZrO_2$-28 were smaller than those of P-$ZrO_2$-66 (133 $m^2\ g^{-1}$ and 0.64 $cm^3\ g^{-1}$), suggesting that partial collapse of the porous structure occurred.

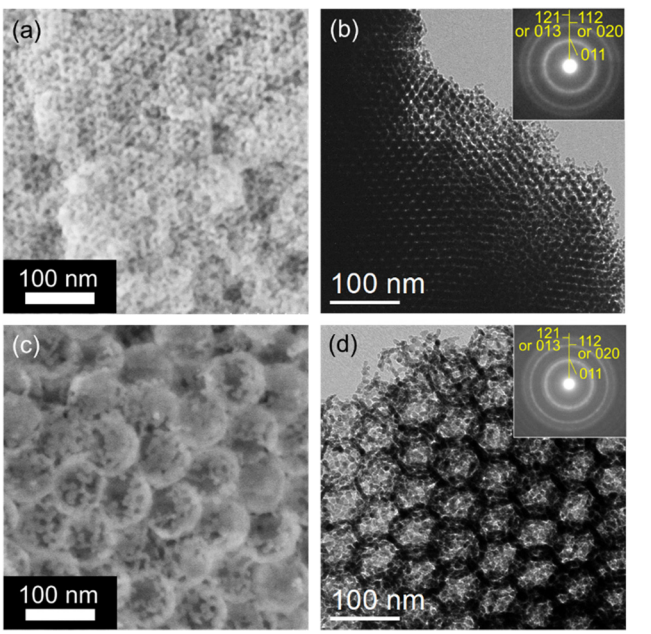


Fig. 6 (a) SEM image and (b) TEM image of P-$ZrO_2$-28 and (c) SEM image and (d) TEM image of P-$ZrO_2$-109 (inset: SAED pattern).

 

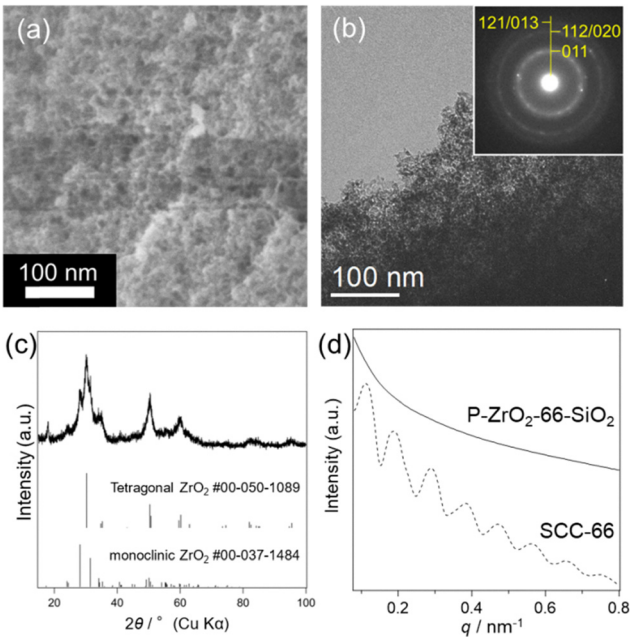


Fig. 7 (a) SEM image, (b) TEM image (inset: SAED pattern), (c) XRD pattern (bottom: simulated patterns), and (d) SAXS pattern of P-$ZrO_2$-66-$SiO_2$.

According to the above results, ordered nanoporous zirconia with fcc-arranged spherical pores ranging from about 16 nm to 82 nm was successfully prepared. The less regular structure observed in P-$ZrO_2$-28 may be due to the large crystallite size relative to the structural period. The crystallite sizes calculated from XRD patterns using the Scherrer equation were approximately 7 nm for P-$ZrO_2$-28, 66, and 109, showing no significant difference. On the other hand, as the structural period decreases, the number of crystallites constituting the pore wall of each spherical pore also decreases. Therefore, in P-$ZrO_2$-28, the reduced number of contact points between crystallites may have resulted in regions where the pore structure could not be maintained.

### Direct preparation of inverse opal zirconia using SCCs as templates

Details of the experimental procedure and characterization are shown in SI. The template was changed to SCCs-66, and the composite sample $SiO_2$-$ZrO_2$-66 was prepared by infiltrating a $Zr(OBu)_4$ solution into the interstitial nanopores of the nanospheres, followed by calcination. The SEM image (Fig. S12a, SI) shows that fine nanoparticles, ranging in size from several to ten nm, were deposited on the surface of the silica nanospheres. The SAXS pattern (Fig. S12b, SI) exhibited little change from that of the original SCCs, and the XRD pattern (Fig. S12c, SI) displayed a halo pattern of silica along with peaks that could be assigned to t-$ZrO_2$. SEM and TEM images of P-$ZrO_2$-66-$SiO_2$ after removal of the template (Fig. 7a and b) revealed random aggregates of microcrystals with no regular spherical pores. The SAED pattern was a ring pattern derived from t-$ZrO_2$, and the XRD pattern (Fig. 7c) confirmed the formation of t-$ZrO_2$ as a major phase and m-$ZrO_2$ as a minor phase. No peaks were observed in the SAXS pattern (Fig. 7d), confirming the absence of regular structures. The BJH pore size distributions from $N_2$ adsorption–desorption measurements also showed no peaks, supporting the formation of irregularly aggregated nanoparticles.

Preparation of ordered nanoporous zirconia using a $ZrOCl\cdot 8H_2O$ precursor was also attempted according to a previous report,[21] but a regular structure was not obtained (Fig. S13, SI). Some regions replicated the porous structure of the template (SEM, Fig. S13c and d, SI), but these were minor. It is possible that unclarified factors in the experimental conditions or the use of silica nanospheres with a size of 28 nm—slightly smaller than the previously reported size (34 nm)[21]—limit the formation of porous structures.

These results show that inverse opal zirconia was not obtained when SCCs were used as a template, supporting the aforementioned discussion on the influence of the templates. Therefore, the present method using carbon as a nanoscale scaffold is significant for controlling porous structures.

### Preparation of mesoporous zirconia using a $ZrOCl_2$ precursor

Significant differences were observed in both the composite and the mesoporous zirconia when $ZrOCl_2$ was used as the zirconium precursor instead of $Zr(OBu)_4$. Although the precursor was deposited on the surface of the pore walls of the carbon template, SEM and TEM images of the composite (C–$ZrO_2$-$ZrOCl_2$) revealed a localized distribution of the precursor (Fig. S14a–c). The localization of zirconium species was further visualized by HAADF-STEM and EDS elemental mapping images (Fig. S14d–g). In the mesoporous zirconia obtained after template removal (P-$ZrO_2$-$ZrOCl_2$), spherical mesopores and crystallization into tetragonal zirconia were confirmed (Fig. S15 and S16a). However, the SAXS pattern (Fig. S16b) exhibited a broader pattern than that of P-$ZrO_2$-66. The $N_2$ adsorption–desorption isotherms and the corresponding pore diameter distributions also indicated a broader pore size distributions (Fig. S16c and d). These results are considered to be caused by the localized deposition of zirconium species, which led to a smaller particle size of mesoporous zirconia and a reduced number of repeating units in the ordered structure. Additionally, the structural collapse is thought to be another contributing factor. Overall, although there remain challenges in controlling structural order, these results demonstrate that mesoporous zirconia reflecting the template nanostructure can be partially obtained, indicating the potential applicability of non-alkoxide precursors in our synthetic method.

## Conclusions

In conclusion, ordered nanoporous zirconias with uniform spherical pores in the range of about 16 to 80 nm were successfully prepared using inverse opal carbon templates and zirconium alkoxide. The uniform coating of the pore walls of nanoporous carbon with zirconium oxide and the crystallization of zirconia subsequent to template removal were crucial for forming the ordered nanoporous structure. The nanoporous

zirconias produced are expected to be useful for catalysts and catalyst supports. In principle, the present method can be applied to other metal oxides and may provide a means to control the pore structure of mesoporous oxides that were difficult to fabricate using silica colloidal crystals as a template.

## Author contributions

T. M. designed the experiment, performed part of the analyses, and wrote the manuscript under the supervision of H. W., A. S., and K. K. G. K. mainly performed the experiments and characterizations.

## Conflicts of interest

There are no conflicts to declare.

## Data availability

The data supporting this article have been included as part of the SI. Supplementary information: Details of comparative experiments, discussions, and characterization; and XRD, SEM, TEM, SAXS, Raman, FT-IR, TG-DTA, $N_2$ adsorption–desorption results. See DOI: **https://doi.org/10.1039/d5nj01465d**.

## Acknowledgements

The authors are grateful to Mr T. Nakaya, Mr A. Sakamoto, Ms S. Nagae, Ms N. Muramoto, and Dr T. Hikino (Waseda University) for the fruitful discussions and Mr S. Enomoto for EM analyses. This work was supported in part by a JST FOREST Program (Grant number JPMJFR2224). Part of the data in this work was obtained using research equipment (JASCO NRS-4100 (C1003), PerkinElmer PE2400II (C1059), Rigaku NANO-Viewer (G1008), JEOL JEM-2010 (G1024), Hitachi S-5500 (G1028), Rigaku RINT Ultima III (G1035), and Quantachrome Autosorb-iQ (G1038)) shared in MEXT Project for promoting public utilization of advanced research infrastructure (Program for supporting construction of core facilities) Grant Number JPMXS04405025.

## References

1 B. Qi, S. Liang, Y. Li, C. Zhou, H. Yu and J. Li, *Adv. Eng. Mater.*, 2022, **24**, 2101278.
2 W. Stichert and F. Schüth, *Chem. Mater.*, 1998, **10**, 2020–2026.
3 A. Navrotsky, *J. Mater. Chem.*, 2010, **20**, 10577–10587.
4 W. Li, H. Huang, H. Li, W. Zhang and H. Liu, *Langmuir*, 2008, **24**, 8358–8366.
5 S. Wang, Y. Fang, Z. Huang, H. Xu and W. Shen, *Catalysts*, 2020, **10**, 262.
6 Y. Zhang, Y. Zhao, T. Otroshchenko, S. Han, H. Lund, U. Rodemerck, D. Linke, H. Jiao, G. Jiang and E. V. Kondratenko, *J. Catal.*, 2019, **371**, 313–324.
7 T. Yamaguchi, *Catal. Today*, 1994, **20**, 199–218.
8 C. A. Nelson, J. R. Szczech, Q. Xu, M. J. Lawrence, S. Jin and Y. Ge, *Chem. Commun.*, 2009, 6607–6609.
9 C. A. Akinnawo, N. Bingwa and R. Meijboom, *Microporous Mesoporous Mater.*, 2021, **311**, 110693.
10 S. Nong, W. Dong, Y. Xiao, M. S. Riaz, C. Dong, Y. Zhao, Z. Liu, R. Wang and F. Huang, *ACS Appl. Nano Mater.*, 2020, **3**, 3315–3322.
11 Y. Chen, S. K. Lunsford, Y. Song, H. Ju, P. Falaras, V. Likodimos, A. G. Kontos and D. D. Dionysiou, *Chem. Eng. J.*, 2011, **170**, 518–524.
12 P. Yang, D. Zhao, D. I. Margolese, B. F. Chmelka and G. D. Stucky, *Nature*, 1998, **396**, 152–155.
13 B. Liu and R. T. Baker, *J. Mater. Chem.*, 2008, **18**, 5200–5207.
14 D. Gu, W. Schmidt, C. M. Pichler, H.-J. Bongard, B. Spliethoff, S. Asahina, Z. Cao, O. Terasaki and F. Schüth, *Angew. Chem., Int. Ed.*, 2017, **56**, 11222–11225.
15 B. T. Holland, C. F. Blanford and A. Stein, *Science*, 1998, **281**, 538–540.
16 X. Sun, J. Liu and Y. Li, *Chem. – Eur. J.*, 2006, **12**, 2039–2047.
17 S. Li, J. Zheng, Y. Zhao and Y. Liu, *J. Porous Mater.*, 2009, **16**, 553–556.
18 C. M. Phillippi and K. S. Mazdiyasni, *J. Am. Ceram. Soc.*, 1971, **54**, 254–258.
19 T. Nomura, S. Tanii, M. Ishikawa, H. Tokumoto and Y. Konishi, *Adv. Powder Technol.*, 2013, **24**, 1013–1016.
20 X. Zheng, Y. Lv, Q. Kuang, Z. Zhu, X. Long and S. Yang, *Chem. Mater.*, 2014, **26**, 5700–5709.
21 D. G. Gregory, Q. Guo, L. Lu, C. J. Kiely and M. A. Snyder, *Langmuir*, 2017, **33**, 6601–6610.
22 Y. Wei, Z. Zhao, X. Yu, B. Jin, J. Liu, C. Xu, A. Duan, G. Jiang and S. Ma, *Catal. Sci. Technol.*, 2013, **3**, 2958–2970.
23 C. Yang, C. Pei, R. Luo, S. Liu, Y. Wang, Z. Wang, Z.-J. Zhao and J. Gong, *J. Am. Chem. Soc.*, 2020, **142**, 19523–19531.
24 A. Taguchi and F. Schüth, *Microporous Mesoporous Mater.*, 2005, **77**, 1–45.
25 X. Deng, K. Chen and H. Tüysüz, *Chem. Mater.*, 2017, **29**, 40–52.
26 K.-M. Choi and K. Kuroda, *Chem. Commun.*, 2011, **47**, 10933–10935.
27 N. Muramoto, T. Matsuno, H. Wada, K. Kuroda and A. Shimojima, *Chem. Lett.*, 2021, **50**, 1038–1040.
28 X. Dong, J. Fu, X. Xiong and C. Chen, *Mater. Lett.*, 2011, **65**, 2486–2488.
29 C. T. Lynch, K. S. Mazdiyasni, J. S. Smith and W. J. Crawford, *Anal. Chem.*, 1964, **36**, 2332–2337.
30 X. Yang, J. Zhang, S. Yang and H. Huang, *Electrochemistry*, 2017, **85**, 2–6.
31 M. Le Toullec, C. J. Simmons and J. H. Simmons, *J. Am. Ceram. Soc.*, 1988, **71**, 219–224.
32 X. Dou, D. Mohan, C. U. PittmanJr. and S. Yang, *Chem. Eng. J.*, 2012, **198**, 236–245.
33 J. van Doorn, J. Varloud, P. Mériaudeau, V. Perrichon, M. Chevrier and C. Gauthier, *Appl. Catal., B*, 1992, **1**, 117–127.
34 M. Stefik, *J. Mater. Res.*, 2022, **37**, 25–42.
35 S. C. Wechsler, A. Gregg, C. S. Collins, S. K. Balijepalli and M. Stefik, *New J. Chem.*, 2025, **49**, 5716–5728.

 